Computational Materials Science 218 (2023) 111954

Contents lists available at ScienceDirect

Computational Materials Science

journal homepage: www.elsevier.com/locate/commatsci

Letter

Elastic investigation for the existence of B33 phase in TiNi shape memory alloys using atomistically informed Eshelby's ellipsoidal inclusion

Akio Ishii

Department of Mechanical Science and Bioengineering, Osaka University, Osaka 560-8531, Japan

ARTICLE INFO

Keywords:
Shape memory alloy
Density functional theory
Eshelby's ellipsoidal inclusion

ABSTRACT

The existence of the B33 phase in TiNi alloys, which was reported to be a stable phase using density functional theory calculations but not confirmed experimentally, is controversial. Using Eshelby's ellipsoidal inclusion, which was atomistically informed by density functional theory calculations, we investigated the existence of the B33 phase in the TiNi shape memory alloy. The calculated total strains of the heterogeneously nucleated B33 phase were similar to the eigenstrains of the B19' phase, which were also calculated using density functional theory calculations. Considering the similarity of the atomic structures of B33 and B19', this indicates that the B33 phase was elastically suppressed and changed to the B19' phase by the original B2 matrix. We confirmed that the elastic inhomogeneity between the B2 matrix and B33 phase plays a role in this change.

Shape memory alloys (SMAs) are alloys with a (1) shape memory effect; plastically deformed SMAs recover their original shape and size when heated above a certain characteristic temperature, (2) superelasticity; plastically deformed SMAs recover once the external load is removed. Because of these properties, SMAs have considerable potential for a wide scope of industrial applications, including in the field of structural materials, actuators, transducers, and sensors [1]. Studies have found that the shape memory effect (superelasticity) is due to the SMA's high phase transformability with respect to heat (external load), from the matrix (parent) phase to the secondary (twin) phase, and vice versa [1]. Nevertheless, the detailed mechanism of plastic deformation remains under investigation.

The near-equal atomic TiNi alloy is the most distinguished SMA [2], for which the observed phase transformation was from cubic B2 matrix to monoclinic B19' secondary phase; one of the edge vectors of the unit cell of the B19' structure has a monoclinic angle larger than 90°. The B19' phase is considered as the most stable secondary phase at, or below, room temperature [3,4]. Meanwhile, the atomistic simulation using the electronic structure calculation of density functional theory (DFT) found a more stable B33 phase (B19' is a metastable structure), which has a larger monoclinic angle than that of B19'. However, this has not been observed in experiments [5–10]. The reason for this discrepancy between the experimental and simulation results remains controversial. Several previous studies have suggested that the reason for this is that the observed B19' phase is stabilized through internal stresses; however, a detailed analysis of the internal stresses is lacking [5,11]. Recently, Haskins et al. [10] discussed the reason for the thermal stability of B19' and B33 using DFT-calculated free energy, which includes vibration entropy. Lv et al. [12] asserted that the reason is due to the effect of the (001) twin interface of the B19' structure using DFT calculations.

In this study, we consider this discrepancy from a micromechanical perspective [13]. In micromechanics, once a secondary phase with eigenstrains (change in shape or size), also called as an inclusion in micromechanics, nucleates heterogeneously in the matrix, internal stress inside the inclusion is generated to push it back to the matrix's original shape (or size). Due to this internal back stress, the observed strains of the inclusion, called as the total strains in micromechanics, is usually lower than the eigenstrains, which can be considered as strains of perfectly homogeneous phase transformation. In other words, the inclusion is elastically deformed back to the shape of the matrix from its original shape by the surrounding matrix. Therefore, DFT-calculated shape changes from the matrix to secondary phase using the homogeneous atomic supercell are eigenstrains, and experimentally observed shape changes are the total strains due to heterogeneity. In this sense, even if the B33 phase nucleates heterogeneously in the B2 matrix, its monoclinic angle will be lower than that of DFT-calculated one. Because the atomic structure of the B19' phase can be considered as an affinely deformed structure of the B33 phase with small shuffling components of internal coordinates [8–10], from a micromechanical perspective, it can be explained as follows. The experimentally observed B19' structure is an elastically deformed B33 structure by the internal back stress by the B2 matrix, or the internal back stress by the B2 matrix totally changes it to the B19' phase. Although we cannot distinguish the above two situations through real

E-mail address: ishii@me.es.osaka-u.ac.jp.

https://doi.org/10.1016/j.commatsci.2022.111954
Received 5 October 2022; Received in revised form 22 November 2022; Accepted 27 November 2022
Available online 7 December 2022

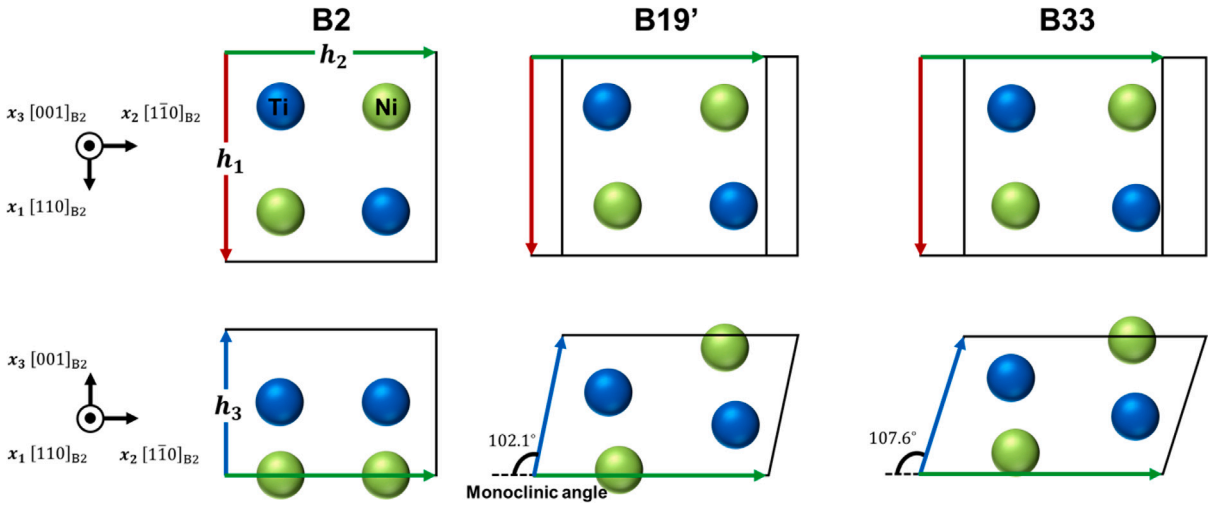

Fig. 1. Atomic structures of the B2 matrix, and the B19' and B33 secondary phases. The units of the supercells include two Ti and two Ni atoms. The supercells used for DFT calculation are shown by black lines and the edge vectors ($\boldsymbol{h}_1$, $\boldsymbol{h}_2$ and $\boldsymbol{h}_3$) of the supercells are shown as red, green, and blue arrows, respectively. The monoclinic angles of the optimized supercells are shown here.

experiments, considering that the B19' phase was also revealed as a metastable structure using atomistic simulation, the latter explanation is more probable.

In the following section, we investigated the validity of the aforementioned explanation using atomistic simulations and micromechanics. We calculated the eigenstrains of B19' and B33 phases, and the elastic constants of B2 and B33 phases using atomistic simulations with DFT calculations. We then predicted the total strains of the B33 phase in the B2 matrix using Eshelby's ellipsoidal inclusion with DFT-calculated eigenstrains and elastic constants. Considering the elastic anisotropy and inhomogeneity of the elastic constants between the B2 matrix and B33 inclusion, an atomistically informed parameter-free analysis was conducted [13–17]. Finally, we compared the predicted total strains of B33 structure and the eigenstrains of B19' structure.

First, we introduce our atomistic simulation and micromechanical approach. Fig. 1 shows the atomic structures of the B2, B19', and B33 phases, which were used in the DFT calculation. The raw data of these atomic structures is available as supplemental material (Vienna Ab initio Simulation Package POSCAR format). The units of the supercells included two Ti and two Ni atoms. The coordinate system was set as $[110]_{B2} - [1\bar{1}0]_{B2} - [001]_{B2}$. After the structural optimization of the DFT calculation, the edge vectors of the supercells $\boldsymbol{h}_1$, $\boldsymbol{h}_2$ and $\boldsymbol{h}_3$, which included the information of lattice constants and monoclinic angle, were calculated for each structure. Subsequently, the cell matrix $\boldsymbol{H}$ was defined as $\boldsymbol{H} \equiv [\boldsymbol{h}_1\ \boldsymbol{h}_2\ \boldsymbol{h}_3]$ for each structure. From Fig. 1, the monoclinic angle of B19' phase (102.1°) is smaller than that of B33 phase (107.6°). As we mentioned above, the heterogeneously nucleated B33 phase will be elastically deformed back to the shape of the B2 matrix from its original shape by the surrounding B2 matrix. The purpose of this study is to confirm that the monoclinic angle of elastically deformed B33 is similar to (or smaller than) that of B19' or not. Using the optimized supercell matrices of the matrix B2 structure, $\boldsymbol{H}_{\mathbf{B2}}$, and the secondary phase, $\boldsymbol{H}_X$ (the subscript X denotes B19' or B33), the eigenstrain of the secondary phases, $\epsilon_{ij}^{\mathrm{X}}$ was computed in the form of Green strain as

$$\epsilon_{ij}^{X} = \frac{1}{2}\left(\boldsymbol{J}_X^{\mathrm{T}}\boldsymbol{J}_X - \boldsymbol{I}\right), \tag{1}$$

where $\boldsymbol{J}_X^{\mathrm{T}} = \boldsymbol{H}_X\left(\boldsymbol{H}_{\mathbf{B2}}\right)^{-1}$ denotes the deformation tensor [17]. For DFT calculations, we used the Vienna Ab initio Simulation Package [18]. The electron–ion interaction in the DFT was described using the projector-augmented wave method [19] and the exchange correlation between electrons was treated using the Perdew–Burke–Ernzerhof generalized gradient approximation [20].

An energy cutoff of 350 eV was used for the plane-wave expansion. A 7 × 7 × 15 k-point mesh was used for all structures. The energy convergence criteria for the electronic and ionic structure relaxations were set to 10^{-8} and 10^{-4} eV, respectively.

Considering the B33 phase in the B2 matrix as an Eshelby ellipsoidal inclusion [14,15], we predicted the total strains of the B33 phase. Specifically, we defined the ellipsoid as $\frac{x_1^2}{a_1^2} + \frac{x_2^2}{a_2^2} + \frac{x_3^2}{a_3^2} = 1$, where a_i was the half axis of the ellipsoid in each direction. We used $(a_1; a_2; a_3) = (10/\sqrt{2}; 10/\sqrt{2}; 1)$ and $(a_1; a_2; a_3) = (1; 1; 10)$ ellipsoids for the disk- and needle-shaped B33 phase, respectively, based on previous experimental and computational observations of the secondary phase in TiNi alloys [21–23]. We then detected the stable morphology, shape and orientation, of the B33 phase with the minimum of elastic energy increment ΔE due to the existence of the B33 phase, and calculated the total strains of the morphology. Although the V-shaped B19' phase was also experimentally observed [4], we did not employ such a shape because of the limitation of Eshelby's ellipsoidal inclusion; ellipsoids cannot mimic such complicated shapes. However, we think that the observed V-shape can be considered as a cluster of simple disks or needles. Note we did not investigate B33 phase in B19' matrix because the matrix phase is always B2 in experiment (not B19'). The nucleation of B33 in B19' phase, intermediate phase transformation, may also occur, but this is out of the scope of this study; we focus on final nucleated structure and it will be B19' or B33 phase in B2 matrix.

For Eshelby's ellipsoidal inclusion, the total strain ε_{ij} is described using the Einstein summation convention [13] as follows:

$$\varepsilon_{kl} = S_{klmn}\epsilon_{mn}, \tag{2}$$

where S_{klmn} denotes Eshelby's tensor [14] and ϵ_{ij} denotes the eigenstrain. Considering the elastic anisotropy of the B2 structure [13,16], S_{klmn} is described as follows:

$$S_{klmn} = \frac{1}{8\pi}C_{pqmn}^{\mathrm{B2}}\int_{-1}^{1} d\zeta_3 \times \int_0^{2\pi}\left(\frac{\xi_l\xi_q N_{kp}(\xi_1,\xi_2,\xi_3) + \xi_k\xi_q N_{lp}(\xi_1,\xi_2,\xi_3)}{D(\xi_1,\xi_2,\xi_3)}\right)d\theta, \tag{3}$$

where

$$D(\xi_1,\xi_2,\xi_3) = P_{pqr}(C_{pj1l}^{\mathrm{B2}}\xi_j\xi_l)(C_{qm2n}^{\mathrm{B2}}\xi_m\xi_n)(C_{rs3t}^{\mathrm{B2}}\xi_s\xi_t),$$

$$N_{km}(\xi_1,\xi_2,\xi_3) = \frac{1}{2}P_{kst}P_{mnr}(C_{sjnl}^{\mathrm{B2}}\xi_l\xi_j)(C_{turv}^{\mathrm{B2}}\xi_u\xi_v),$$

corresponding to the determinant and cofactor of $K_{km} = C_{klmn}^{\mathrm{B2}}\xi_l\xi_n$, respectively. C_{ijkl}^{B2} is the elastic constant of the B2 matrix and P_{pqr}

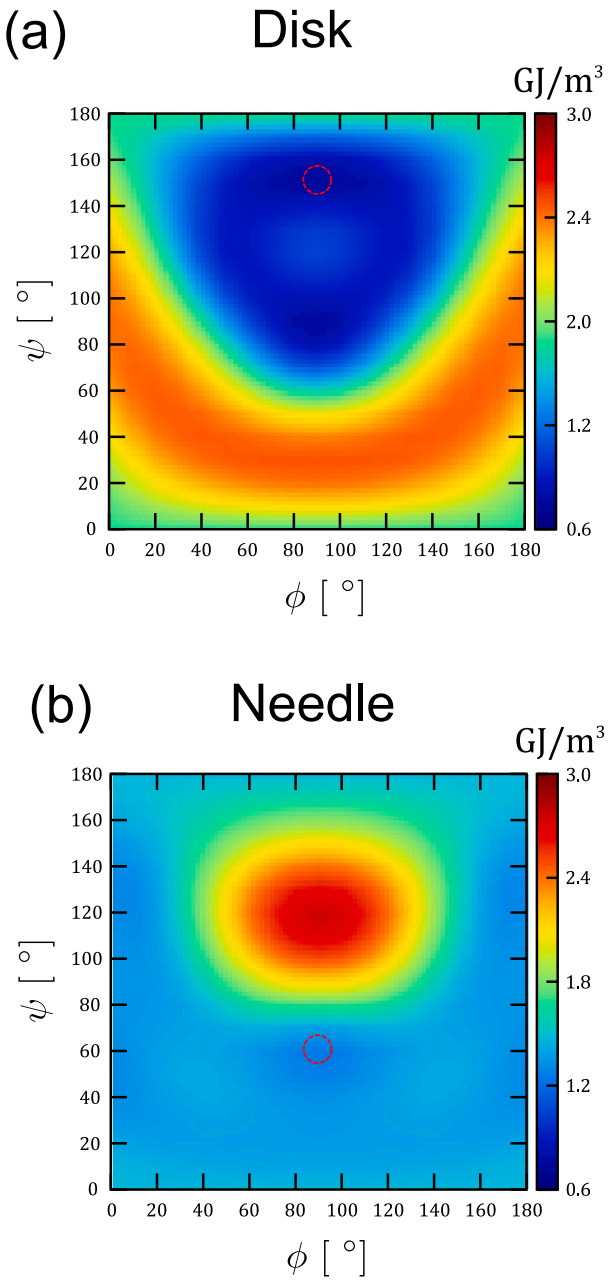

Fig. 2. Elastic energy increment ΔE changes with respect to ϕ and ψ for (a) disk and (b) needle ellipsoidal inclusions. Broken circles indicate the area with the minimum ΔE for each case.

denotes the permutation tensor. Using ζ_3 and θ, $[\xi_1;\xi_2;\xi_3]$ can be described as

$$\begin{bmatrix}\xi_1\\ \xi_2\\ \xi_3\end{bmatrix} = \begin{bmatrix}\frac{\sqrt{1-\zeta_3^2}\cos\theta}{a_1}\\ \frac{\sqrt{1-\zeta_3^2}\sin\theta}{a_2}\\ \frac{\zeta_3}{a_3}\end{bmatrix}.$$

The inhomogeneity of the elastic constant between the B2 matrix and B33 phase can be considered using Eshelby's equivalent inclusion theory [13,15]. The fictitious strain $\tilde{\epsilon}_{ij}$ was calculated using the following equation:

$$C^{\mathrm{B33}}_{ijkl}(S_{klmn}\tilde{\epsilon}_{mn} - \epsilon^{\mathrm{B33}}_{kl}) = C^{\mathrm{B2}}_{ijkl}(S_{klmn}\tilde{\epsilon}_{mn} - \tilde{\epsilon}_{kl}), \quad (4)$$

where C^{B33}_{ijkl} is the elastic constant of the B33 phase. Next, the total strains of the B33 phase were calculated as $\epsilon^{\mathrm{B33}}_{kl} = S_{klmn}\tilde{\epsilon}_{mn}$ using Eq. (2). Using the total strains and eigenstrains of the B33 phase, the internal stress of the B33 phase σ_{ij} was calculated as

$$\sigma_{ij} = C^{\mathrm{B2}}_{ijkl}(\epsilon^{\mathrm{B33}}_{kl} - \tilde{\epsilon}_{kl}). \quad (5)$$

Finally, the elastic energy increment ΔE due to the existence of the B33 phase in the B2 matrix was described as

$$\Delta E = -\frac{1}{2}\sigma_{ij}\epsilon^{\mathrm{B33}}_{ij}. \quad (6)$$

The change of the orientation of the B33 phase was considered by changing the coordinate system of the eigenstrains and elastic constants from the original $\boldsymbol{x_1}-\boldsymbol{x_2}-\boldsymbol{x_3}$ to $\boldsymbol{x'_1}-\boldsymbol{x'_2}-\boldsymbol{x'_3}$ using the following rotation matrix [17,24]:

$$R_{ij} = \begin{bmatrix}\cos\psi\cos\phi & \cos\psi\sin\phi & -\sin\psi\\ -\sin\phi & \cos\phi & 0\\ \sin\psi\cos\phi & \sin\psi\sin\phi & \cos\psi\end{bmatrix}. \quad (7)$$

The $\boldsymbol{x'_3}$ axis was perpendicular to the disk and parallel to the longitude of the needle in our setting. By changing the angles of ϕ ($0° < \phi < 180°$) and ψ ($0° < \psi < 180°$) for the disk and needle, respectively, we detected the shape and orientation with the minimum of ΔE as the stable morphology of the B33 phase, and calculated its total strains $\epsilon^{\mathrm{B33}}_{ij}$. The details of our method and its fundamental physics were covered by previous studies [13,17]. Further, the elastic constants of the B2 matrix, and B19' and B33 phases were calculated by computing the Hessian matrix using their supercells with DFT calculations [25,26]. The relaxation of internal coordinates is not considered for the calculation of elastic constants. The elastic constants of the B19' phase were calculated to provide the data for the subsequent mesoscale analysis, such as the phase-field method.

The calculated eigenstrains for each structure together with those calculated using previously reported lattice parameters and the monoclinic angle are shown in Table 1. The elastic constants for each structure are shown in Table 2. The calculated eigenstrains were generally consistent with those calculated in previous studies, and the calculated elastic constants of the B2 matrix were also consistent with the previous DFT results, i.e., $C_{2323} = C_{3131} = 46$ GPa and $C_{1212} = 19$ GPa [11]. The corresponding values of C_{1111}, C_{1122} and C_{2323} triplet on conventional $[100]_{\mathrm{B2}}-[010]_{\mathrm{B2}}-[001]_{\mathrm{B2}}$ coordinate system for B2 case are 179, 152 and 52 GPa, respectively, which are consistent with those of material project [27] and similar to previous experimental results: approximately 175, 150 and 32 GPa at 300 K [28]. Notably, the shear components of the elastic constants, C_{2323}, C_{3131}, and C_{1212} of the B2 matrix, and those of the B33 or B19' phases are significantly different; the elastic inhomogeneity between the B2 matrix and the B33 or B19' phase exists, which needs to be considered. We confirmed the temperature effect for the elastic constants is small and it does not change the conclusion of this research using phonon analysis under quasi harmonic approximation [29]. In Fig. 2, the ΔE maps with respect to ϕ and ψ for (a) disk and (b) needle shapes are shown. Generally, the disk shape is more stable than the needle shape; in particular, ΔE is low for the disk in the region ($60° < \phi < 120°, 140° < \psi < 160°$). If we consider the experimental habit plane as the disk plane in this study, this is consistent with previous experimental observations. The habit plane of the B19' phase, $(249)_{\mathrm{B2}}$ [4,23], approximately corresponded to the disk with an angle $(\phi,\psi) = (80°, 150°)$.

The minimum of ΔE was at $(90°, 150°)$ for the disk shape, i.e., $\Delta E = 0.74$ GJ/m^3. The total strains of the disk, $(\phi,\psi) = (90°, 150°)$, were calculated as $\epsilon^{\mathrm{B33}}_{11} = -0.014$, $\epsilon^{\mathrm{B33}}_{22} = 0.126$, $\epsilon^{\mathrm{B33}}_{33} = -0.013$, and $\epsilon^{\mathrm{B33}}_{23} = 0.114$, which are similar to the eigenstrains of the B19' phase in Table 1. Using $\epsilon^{\mathrm{B33}}_{23}$, the monoclinic angle of the elastically deformed B33 phase was approximately calculated as $90° + \arctan(2\epsilon^{\mathrm{B33}}_{23}) = 102.8°$, which is similar to that of B19', i.e., 102.1° (see Fig. 1). Thus, although we did not consider the elastic instability of the B33 phase in our micromechanics analysis, we believe that the B33 structure reaches instability

Table 1
Eigenstrains of B19' and B33 phases calculated using atomistic simulation with DFT calculation. Note that $\epsilon_{ij} = \epsilon_{ji}$ and the values of the other ϵ_{ij} not listed are zeros. For the comparison, the eigenstrain calculated using previous reported lattice constants and monoclinical angles are also included.

	ϵ_{11}	ϵ_{22}	ϵ_{33}	ϵ_{23}
B19′				
This work	−0.059	0.121	−0.009	0.116
Expt [3]	−0.035	0.096	−0.035	0.072
DFT [6]	−0.050	0.135	−0.030	0.117
DFT [7]	−0.047	0.132	−0.030	0.095
DFT [9]	−0.052	0.127	−0.022	0.112
B33				
This work	−0.061	0.163	−0.013	0.172
DFT [5]	−0.059	0.173	−0.023	0.166
DFT [6]	−0.056	0.161	−0.028	0.160
DFT [7]	−0.053	0.171	−0.030	0.167
DFT [9]	−0.057	0.169	−0.026	0.167

Table 2
Elastic constants of B2, B19', and B33 phases calculated using atomistic simulation with DFT calculation. Note that $C_{ijkl} = C_{jikl} = C_{ijlk} = C_{klij}$ and the values of other C_{ijkl} not listed are zeros. The unit of the elastic constants is GPa. The elastic constants are defined in $[110]_{B2} - [1\bar{1}0]_{B2} - [001]_{B2}$ coordinate system.

Elastic constant	B2	B19′	B33
C_{1111}	215	237	235
C_{2222}	215	231	234
C_{3333}	179	182	178
C_{1122}	116	129	130
C_{1133}	143	132	135
C_{2233}	143	118	113
C_{2323}	52	44	36
C_{3131}	52	87	87
C_{1212}	13	91	93
C_{1123}	0	−3	−1
C_{2223}	0	21	23
C_{3323}	0	−2	−3
C_{3112}	0	3	3

and changes to the B19' phase, releasing the internal stresses. In real experiments, this is a reasonable scenario for heterogeneous secondary phases because the main difference between the atomic structures of the B33 and B19' phases is the shape of the supercell as we mentioned previously. Only small internal atomic shuffling (the change in internal coordinates) [30] are necessary for this phase transformation. For the detail, the reader can refer our supplemental data of B33 and B19' atomic structure. As further investigation, we recalculated the ΔE map *without* elastic inhomogeneity, setting $C^{B33}_{ijkl} = C^{B2}_{ijkl}$. In this case, we found that the morphology did not change, and the calculated total strains were $\epsilon^{B33}_{11} = -0.015$, $\epsilon^{B33}_{22} = 0.148$, $\epsilon^{B33}_{33} = -0.025$, and $\epsilon^{B33}_{23} = 0.134$, which were larger than the eigenstrains of B19'; the monoclinic angle was approximately calculated as 105.0°, indicating that the elastic deformation is relatively suppressed compared with the above case. Thus, the elastic inhomogeneity between the B2 matrix and B33 phase is important to suppress the B33 phase. Note we think our suggestion does not conflict Lv et al.'s assertion; twinned structure stabilizes the B19' phase [12]. If the twin region exists heterogeneously, both matrix and twin region will be constrained elastically due to the twin's eigenstrains because the twinning deformation is also one of phase transformations with eigenstrains. Although it is difficult to distinguish the elastic and chemical effect from DFT result, even layered model like Lv et al.'s twinned supercell also includes this kind of elastic constraint.

Additionally, we also calculated the ΔE map with a heterogeneous B19' phase using the eigenstrains and elastic constants of the B19' phase in Tables 1 and 2, and assumed that the B19' phases nucleate heterogeneously in the B2 matrix, which would be the actual situation of the experiment from the above discussion. We found that the morphology did not change for the B33 cases and calculated the total strains as $\epsilon^{B19'}_{11} = -0.013$, $\epsilon^{B19'}_{22} = 0.093$, $\epsilon^{B19'}_{33} = -0.016$, and $\epsilon^{B19'}_{23} = 0.082$, which were similar to the B19' eigenstrains, calculated using the experimental value (see Table 1). The monoclinic angle was approximately calculated as $90° + \arctan(2\epsilon^{B19'}_{23}) = 99.3°$, and the experimental value was 97.9° [3]. Considering the effect of the heterogeneity of the B19' phase in the experiment, the discrepancy in the experimental results and DFT calculations of the B19' phase's monoclinic angle could be explained.

In summary, we investigated the existence of the B33 phase in TiNi SMAs using Eshelby's ellipsoidal inclusion, which were atomistically informed by DFT calculations. The calculated total strains of the heterogeneously nucleated B33 phase were similar to the eigenstrains of the B19' phase, which were calculated using DFT calculations. Considering that the B19' phase is an affinely deformed B33 phase, we concluded that the B33 phase was elastically suppressed and changed to the B19' phase by the original B2 matrix. The inhomogeneity of the elastic constants between the B2 matrix and B33 phase plays a role in this phase change. Finally, the discrepancy in the experiment and DFT calculations of the B19' phase's monoclinic angle was due to the B19' phase's heterogeneity.

CRediT authorship contribution statement

Akio Ishii: Conceptualization, Methodology, Validation, Investigation, Writing – original draft, Writing – review & editing, Visualization, Funding acquisition.

Declaration of competing interest

The authors declare that they have no known competing financial interests or personal relationships that could have appeared to influence the work reported in this paper.

Data availability

Data will be made available on request.

Acknowledgments

This work was partially supported by the Japan Society for the Promotion of Science (JSPS) [grant number 21K03771]. DFT simulations were partly performed using OCTOPUS large-scale computer systems at the Cybermedia Center, Osaka University.

Appendix A. Supplementary data

Supplementary material related to this article can be found online at https://doi.org/10.1016/j.commatsci.2022.111954.

References

[1] J. Mohd Jani, M. Leary, A. Subic, M.A. Gibson, A review of shape memory alloy research, applications and opportunities, Mater. Des. 56 (2014) 1078–1113.
[2] W.J. Buehler, J.V. Gilfrich, R.C. Wiley, Effect of low-temperature phase changes on the mechanical properties of alloys near composition TiNi, J. Appl. Phys. 34 (1963) 1475–1477.
[3] S.D. Prokoshkin, A.V. Korotitskiy, V. Brailovski, S. Turenne, I.Y. Khmelevskaya, I.B. Trubitsyna, On the lattice parameters of phases in binary Ti-Ni shape memory alloys, Acta Mater. 52 (2004) 4479–4492.
[4] M. Nishida, T. Nishiura, H. Kawano, T. Inamura, Self-accommodation of B19' martensite in Ti-Ni shape memory alloys-Part I. Morphological and crystallographic studies of the variant selection rule, Phil. Mag. 92 (2012) 2215–2233.
[5] X. Huang, G.J. Ackland, K.M. Rabe, Crystal structures and shape-memory behaviour of NiTi, Nature Mater. 2 (2003) 307–311.
[6] K. Guda Vishnu, A. Strachan, Phase stability and transformations in NiTi from density functional theory calculations, Acta Mater. 58 (2010) 745–752.
[7] D. Holec, M. Friák, A. Dlouhý, J. Neugebauer, Ab initio study of pressure stabilized NiTi allotropes: Pressure-induced transformations and hysteresis loops, Phys. Rev. B 84 (2011) 224119.

[8] J.B. Haskins, A.E. Thompson, J.W. Lawson, Ab initio simulations of phase stability and martensitic transitions in NiTi, Phys. Rev. B 94 (2016) 214110.
[9] W.S. Ko, B. Grabowski, J. Neugebauer, Development and application of a Ni-Ti interatomic potential with high predictive accuracy of the martensitic phase transition, Phys. Rev. B 92 (2015) 134107.
[10] J.B. Haskins, H. Malmir, S.J. Honrao, L.A. Sandoval, J.W. Lawson, Low-temperature mechanical instabilities govern high-temperature thermodynamics in the austenite phase of shape memory alloy constituents: Ab initio simulations of NiTi, NiZr, NiHf, PdTi, and PtTi, Acta Mater. 212 (2021) 116872.
[11] N. Hatcher, O.Y. Kontsevoi, A.J. Freeman, Martensitic transformation path of NiTi, Phys. Rev. B 79 (2009) 020202.
[12] C. Lv, G. Wang, X. Zhang, B. Luo, N. Luo, H. Song, F. Wu, H. Wu, F. Tan, J. Zhao, C. Liu, C. Sun, New explanation for the existence of B19' phase in NiTi alloy from the perspective of twinning martensite, Scr. Mater. 214 (2022) 114644.
[13] T. Mura, Micromechanics of Defects in Solids, Martinus Nijhoff Publishers, Boston, 1987.
[14] J.D. Eshelby, The determination of the elastic field of an ellipsoidal inclusion, and related problems, Proc. R. Soc. Lond. Ser. A Math. Phys. Eng. Sci. 241 (1957) 376–396.
[15] J.D. Eshelby, Elastic inclusions and inhomogeneities, Prog. Sol. Mech. 2 (1961) 89–140.
[16] N. Kinoshita, T. Mura, Elastic fields of inclusions in anisotropic media, Phys. State Solidi (A) 5 (1971) 759–768.
[17] A. Ishii, *Ab* Initio morphology prediction of Zr hydride precipitates using atomistically informed Eshelby's ellipsoidal inclusion, Comput. Mater. Sci. 211 (2022) 111500.
[18] G. Kresse, J. Furthmüller, Efficient iterative schemes for ab initio total-energy calculations using a plane-wave basis set, Phys. Rev. B 54 (1996) 11169–11186.
[19] G. Kresse, D. Joubert, From ultrasoft pseudopotentials to the projector augmented-wave method, Phys. Rev. B 59 (1999) 1758–1775.
[20] J. Perdew, K. Burke, M. Ernzerhof, Generalized gradient approximation made simple, Phys. Rev. Lett. 77 (1996) 3865–3868.
[21] D. Li, L. Chen, Morphological evolution of coherent multi-variant $Ti_{11}Ni_{14}$ precipitates in Ti-Ni alloys under an applied stress–a computer simulation study, Acta Mater. 46 (1998) 639–649.
[22] Z.K. Lu, G.J. Weng, Two-level micromechanical theory for a shape-memory alloy reinforced composite, Int. J. Plast. 16 (2000) 1289–1307.
[23] H. Sehitoglu, I. Karaman, R. Anderson, X. Zhang, K. Gall, H. Maier, Y. Chumlyakov, Compressive response of NiTi single crystals, Acta Mater. 48 (2000) 3311–3326.
[24] M. Kato, T. Fujii, S. Onaka, Elastic strain energies of sphere, plate and needle inclusions, Mater. Sci. Eng. A 211 (1996) 95–103.
[25] Y. Le Page, P. Saxe, Symmetry-general least-squares extraction of elastic data for strained materials from *ab initio* calculations of stress, Phys. Rev. B 65 (2002) 104104.
[26] X. Wu, D. Vanderbilt, D.R. Hamann, Systematic treatment of displacements, strains, and electric fields in density-functional perturbation theory, Phys. Rev. B 72 (2005) 035105.
[27] A. Jain, S.P. Ong, G. Hautier, W. Chen, W.D. Richards, S. Dacek, S. Cholia, D. Gunter, D. Skinner, G. Ceder, K.A. Persson, Commentary: The materials project: A materials genome approach to accelerating materials innovation, APL Mater. 1 (2013) 011002.
[28] X. Ren, N. Miura, J. Zhang, K. Otsuka, K. Tanaka, M. Koiwa, T. Suzuki, Y.I. Chumlyakov, M. Asai, A comparative study of elastic constants of Ti-Ni based alloys prior to martensitic transformation, Mater. Sci. Eng. A 312 (2001) 196–206.
[29] U. Argaman, G. Makov, First-principles study of the temperature dependence of the elastic constants of hcp titanium, Comput. Mater. Sci. 184 (2020) 109917.
[30] A. Ishii, J. Li, S. Ogata, Shuffling-controlled versus strain-controlled deformation twinning: The case for HCP Mg twin nucleation, Int. J. Plast. 82 (2016) 32–43.